Article

High-Temperature Methane Sensors Based on ZnGa$_2$O$_4$:Er Ceramics for Combustion Monitoring

Aleksei V. Almaev [1,2], Zhakyp T. Karipbayev [3,*], Askhat B. Kakimov [3], Nikita N. Yakovlev [1],
Olzhas I. Kukenov [1], Alexandr O. Korchemagin [1], Gulzhanat A. Akmetova-Abdik [3,*], Kuat K. Kumarbekov [3],
Amangeldy M. Zhunusbekov [3], Leonid A. Mochalov [4,5], Ekaterina A. Slapovskaya [4], Petr M. Korusenko [6,7],
Aleksandra V. Koroleva [8], Evgeniy V. Zhizhin [8] and Anatoli I. Popov [3,9]

[1] Laboratory of Metal Oxide Semiconductors, Research and Development Center for Advanced Technologies in Microelectronics, National Research Tomsk State University, Tomsk 634050, Russia; almaev_alex@mail.ru (A.V.A.); nik_mr_x@mail.ru (N.N.Y.); okukenov@mail.ru (O.I.K.); alexandr.korchemagin@gmail.com (A.O.K.)
[2] Fokon LLC, Kaluga 248035, Russia
[3] Institute of Physical and Technical Sciences, L.N. Gumilyov Eurasian National University, Astana 010008, Kazakhstan; kakimov_ab_2@enu.kz (A.B.K.); kumarbekov_kk_1@enu.kz (K.K.K.); zhunusbekov_am@enu.kz (A.M.Z.); popov@latnet.lv (A.I.P.)
[4] Department of Inorganic Compounds Chemistry, N.I. Lobachevsky State University, Nizhny Novgorod 603950, Russia; mochalovleo@gmail.com (L.A.M.); slapovskaya@unn.ru (E.A.S.)
[5] Department of Physics & Optical Science, The University of North Carolina at Charlotte, Charlotte, NC 28223, USA
[6] Department of Solid-State Electronics, Saint Petersburg State University, Saint Petersburg 199034, Russia; korusenko_petr@mail.ru
[7] Department of Physics, Omsk State Technical University, Omsk 644050, Russia
[8] Research Park, Saint Petersburg State University, Saint Petersburg 199034, Russia; koroleva.alexandra.22@gmail.com (A.V.K.); evgeniy.zhizhin@spbu.ru (E.V.Z.)
[9] Institute of Solid State Physics, University of Latvia, 8 Kengaraga, LV-1063 Riga, Latvia
* Correspondence: karipbayev_zht_1@enu.kz (Z.T.K.); gulzhanatakhmet@gmail.com (G.A.A.-A.)

Abstract

The use of CH$_4$ as an energy source is increasing every day. To increase the efficiency of CH$_4$ combustion and ensure that the equipment meets ecological requirements, it is necessary to measure the CH$_4$ concentration in the exhaust gases of combustion systems. To this end, sensors are required that can withstand extreme operating conditions, including temperatures of at least 600 °C, as well as high pressure and gas flow rate. ZnGa$_2$O$_4$, being an ultra-wide bandgap semiconductor with high chemical and thermal stability, is a promising material for such sensors. The synthesis and investigation of the structural and CH$_4$ sensing properties of ceramic pellets made from pure and Er-doped ZnGa$_2$O$_4$ were conducted. Doping with Er leads to the formation of a secondary Er$_3$Ga$_5$O$_{12}$ phase and an increase in the active surface area. This structural change significantly enhanced the CH$_4$ response, demonstrating an 11.1-fold improvement at a concentration of 10^4 ppm. At the optimal response temperature of 650 °C, the Er-doped ZnGa$_2$O$_4$ exhibited responses of 2.91 a.u. and 20.74 a.u. to 100 ppm and 10^4 ppm of CH$_4$, respectively. The Er-doped material is notable for its broad dynamic range for CH$_4$ concentrations (from 100 to 20,000 ppm), low sensitivity to humidity variations within the 30–70% relative humidity range, and robust stability under cyclic gas exposure. In addition to CH$_4$, the sensitivity of Er-doped ZnGa$_2$O$_4$ to other gases at a temperature of 650 °C was investigated. The samples showed strong responses to C$_2$H$_4$, C$_3$H$_8$, C$_4$H$_{10}$, NO$_2$, and H$_2$, which, at gas concentrations of 100 ppm, were higher than the response to CH$_4$ by a factor of 2.41, 2.75, 3.09, 1.16, and 1.64, respectively. The study proposes a plausible mechanism explaining the sensing effect of Er-doped ZnGa$_2$O$_4$ and discusses its potential for developing high-temperature CH$_4$

sensors for applications such as combustion monitoring systems and determining the ideal fuel/air mixture.

1. Introduction

CH_4 is a colorless and odorless gas. It is a major component of natural gas and a potent greenhouse gas [1,2]. Given the widespread use of CH_4 in industry and households as an energy source, there is a need to increase the efficiency of CH_4 combustion and ensure that the equipment meets ecological requirements, it is necessary to measure the CH_4 concentration in the exhaust gases of combustion systems. To this end, sensors are required that can withstand extreme operating conditions, including temperatures of at least 600 °C, as well as high pressure and gas flow rates. Most sensor electronics materials, metal oxides, and chalcogenides cannot function reliably at temperatures above 600 °C [3–5]. Previously, high-temperature CH_4 sensors based on thin Ga_2O_3 [6,7] and thick $LaFe_{0.95}W_{0.05}O_3$ films [8] were investigated. However, these sensors were not highly sensitive and/or were produced using film deposition methods that are not highly reproducible. There is a need to develop new materials for high-temperature CH_4 sensors that can be produced using relatively inexpensive methods.

Zinc gallate ($ZnGa_2O_4$), being an ultra-wide bandgap semiconductor with high chemical and thermal stability, is a promising material for high-temperature sensors. It possesses a spinel-type crystal structure [9,10]. The band gap width, E_g, of $ZnGa_2O_4$ depends significantly on the synthesis conditions, a presence of impurities and subsequent treatments, and is reported within a relative range of 4.1–5.2 eV [9–14]. To date, $ZnGa_2O_4$ has been shown to be of interest in several areas of electronics and photonics as a material for transparent-conducting electrodes [15], luminophores films [16,17], solar-blind UV detectors with high speed-performance [18,19], power electronics devices [20,21], and gas sensors [11,22]. The last application field is practically not well-developed due to the absence of cost-effective and high deposition rates methods for $ZnGa_2O_4$ synthesis as well as for fabrication of structures on its basis with large active surface. It is particularly difficult to obtain $ZnGa_2O_4$ compounds with the appropriate spinel crystal lattice. The literature analysis summarized in Table 1 shows that, despite these obstacles, sensors based on $ZnGa_2O_4$ capable of functioning in a wide temperature range and demonstrating high responses to nitrogen oxides and volatile hydrocarbon vapors in the operating temperature range of T = 300–450 °C have been developed. The very limited number of literature sources does not yet allow us to draw some general conclusions about the advantages and disadvantages of $ZnGa_2O_4$ as a sensitive material for gas sensors in comparison with the well-developed binary metal-oxide semiconductors (MOSs) SnO_2, ZnO, TiO_2, WO_3, Ga_2O_3 [23–35], or transition metal dichalcogenides (TMDs) [5,36].

The characteristics of $ZnGa_2O_4$-based gas sensors, including gas response and speed-performance, can be controlled by forming arrays of nanoscale structures, changing the topology of contacts to the semiconductor layer, forming heterostructures, and depositing metal-catalyst nanoclusters on the semiconductor surface [11,12,22,37–41].

Table 1. Comparison of gas-sensitive characteristics of $ZnGa_2O_4$-based structures.

Material	Gas	Gas Concentration (ppm)	Temperature (°C)	Response (a.u.)	Refs.
$ZnGa_2O_4$ thin films	NO	6.25	300	22.21	[11]
$ZnGa_2O_4$	LPG *	50	340	7.9	[12]
$ZnGa_2O_4$ nanorods	NO$_2$	10	300	2.85	[22]
$ZnGa_2O_4$-core/TiO_2-shell nanorods				8.76	
$ZnGa_2O_4$ thin films	NO	10	300	11.647	[37]
$ZnGa_2O_4$	LPG *	1000	25	1.32	[38]
$ZnGa_2O_4$/Graphene				1.56	
$ZnGa_2O_4$ thin films	C_2H_4O	300	450	1450	[39]
$ZnGa_2O_4$:N thin films			400	11,000	
$ZnGa_2O_4$-core/ZnO-shell nanowires	NO$_2$	5	250	12	[40]
$ZnGa_2O_4$ nanowires	NO$_2$	5	25 + ultraviolet exposure	2.91	[41]
$ZnGa_2O_4$ nanowires with Au nanoparticles				8.61	

* LPG is the liquid petroleum gas.

A Taguchi-type sensor based on $ZnGa_2O_4$, obtained by solid state reaction assisted by high-energy ball-milling of a mixture of GaOOH and ZnO powders at room temperature (RT) for 7 h and with a periodic addition of ethanol as a lubricant, was presented in Ref. [12]. A paste was formed from the obtained powder and deposited in a thin layer on a ceramic tube, inside of which a heater was formed. The signal from the sensing layer was picked up by means of gold electrodes formed to the semiconductor. The Taguchi-type sensors with a sensitive SnO_2 layer have been manufactured since the late 1960s and are reliable and stable devices with a low base resistance [42], but still exhibit some disadvantages as discussed in Ref. [43]. The use of inexpensive and easy-to-implement ceramic technologies for the synthesis of $ZnGa_2O_4$, similar to the one described in Ref. [12], is promising. However, there is practically no published report devoted to the study of gas-sensitive properties of such materials.

Actually, Refs. [11,37] report on the development and study of sensors based on $ZnGa_2O_4$ with high sensitivity to NO compared to other gases. These sensors can be considered quasi-selective. The authors proposed a mechanism according to which there is a special type of dangling bonds on the surface of $ZnGa_2O_4$, which are effective adsorption centers for NO. Their sensors practically did not respond to CO_2, CO, and SO_2, but showed a much lower response to NO_2 than to NO. High responses of $ZnGa_2O_4$-based sensors to NO_2 exposures were reported in Refs. [22,40,41] as well as by the utilization of the well-known method of increasing the sensitivity and selectivity of MOSs—exposure to ultraviolet radiation [41]. In turn, a few papers have shown a high sensitivity of $ZnGa_2O_4$ to LPG. The responses to LPG are comparable to the responses to NO_x or much higher, which was obtained for sensors based on thin films of $ZnGa_2O_4$ and $ZnGa_2O_4$:N at $T = 450\,°C$ and $400\,°C$, respectively [39]. High sensitivity to NO_x is typical of many MOSs with a number of advantages and disadvantages [44,45]. Indeed, there is much less work done on the development of sensors for volatile hydrocarbon vapors, including LPG [46]. The reason for the high sensitivity of $ZnGa_2O_4$ to LPG is still not clear and is not considered in detail in these papers. The LPG is a mixture of several hydrocarbons like CH_4, C_3H_8, C_4H_{10}, etc. [12,46]. Therefore, it is reasonable to investigate the gas-sensitive properties of $ZnGa_2O_4$ under exposure to the LPG components separately to gain inside into the sensory mechanisms of $ZnGa_2O_4$ and to design highly sensitive and selective sensors. In

this research, we focus on the investigation of the gas-sensitive properties of $ZnGa_2O_4$ upon exposure to CH_4, which is highly relevant to environment quality monitoring and combustion monitoring systems.

More specifically, our research is devoted to the development and investigation of CH_4 sensors based on $ZnGa_2O_4$ and $ZnGa_2O_4$ with Er addition ceramics. It is important to note that the doping of $ZnGa_2O_4$ with various impurities is widely used and studied in detail for the development of effective luminescent materials [13,47–55]; however, to the best of our knowledge, there is not any publication dealing with gas-sensitive properties of $ZnGa_2O_4$ with Er additive. It has been shown that doping with high concentrations of Er-nanostructured SnO_2 [56] and $BiFeO_3$ [57] allows for high responses to alcohol and acetone vapors. At the same time, the sensors are characterized by the long-term stability of gas-sensitive characteristics. Moreover, the method employed in our study for the synthesis of $ZnGa_2O_4$ is characterized by relative simplicity and low cost.

Various types of sensor [1,58–61] are being developed and used to detect CH_4, including optical, calorimetric, pyroelectric, electrochemical, and chemoresistive sensors. Those based on MOSs and TDMs are of particular interest due to their low production cost, miniaturization potential, and compatibility with microelectronic technologies and materials [1,58–61]. Many sensors have been developed to date, mainly based on SnO_2, ZnO and TiO_2, including commercial samples. However, research is ongoing to solve several issues, such as reducing the power consumed by sensors, increasing selectivity, stability, and speed performance, reducing the effect of ambient humidity and detection limits. At the same time, methods of "green manufacturing" for producing sensory materials are being actively considered. In order to address these issues, the investigation of MOSs and methods for modifying their gas-sensitive properties, as well as the study of heterostructures and nanostructures based on MOSs and other semiconductors, is ongoing. Additionally, new materials such as p-type MOSs, TMDs, and various allotropic forms of carbon, along with heterostructures based on these materials, are being employed [1,5,30–35,58–62]. Furthermore, improvements to sensor design are being made. It is worth noting that these studies practically do not consider the development of high-temperature CH_4 sensors.

2. Materials and Methods

Raw materials of Ga_2O_3 (99.99%) and ZnO (99.99%) powders in the stoichiometric ratio were used to synthesize the samples. To introduce Er into the samples, 5 wt% of Er_2O_3 (99.99%) powder was added to the charge. The charge preparation process involved the careful grinding and homogenization in the Tencan XQM-0.4A alundum ball (Changsha Tianchuang Powder Technology Company Limited, Changsha, China) mill for 30 min to ensure the uniform distribution of powder particles. The resulting powder mixtures were compressed at a pressure of 1 MPa into ~1 mm thick pellets. After pressing, the ceramic pellets were subjected to annealing at a temperature of 1500 °C in an air stream for 10 h. The samples were annealed in alundum crucibles, which ensure high-temperature resistance and chemical inertness. The temperature regime was maintained using a high-precision controller. The samples without Er_2O_3 addition were denoted as ZGO and the samples with Er_2O_3 addition—ZGO+Er. All samples presented in this work were synthesized by participants from L.N. Gumilyov Eurasian National University.

X-ray diffraction (XRD) analysis was performed to determine the phase composition of the samples using Bruker D6 PHASER(Bruker Corp., Bremen, Germany) with monochromatic $CuK_{\alpha 1}$ radiation (1.5406 Å). Phase identification was performed using the ICDD database (PDF-4+ 2019). The lattice parameters were estimated using the Rietveld method in the Match4 program. The Williamson–Hall method was used to analyze the broadening of XRD peaks to estimate crystallite size D_c and microstrain ε in materials.

The survey and core-level (Ga $2p_{3/2}$, Zn $2p_{3/2}$, O $1s$, Er $4d$) photoelectron (PE) spectra, recorded using an ESCAlab 250Xi X-ray photoelectron spectrometer (Thermo Fisher Scientific, Oxford, UK) equipped with a monochromatic Al Kα X-ray source ($h\nu$ = 1486.6 eV). The chemical states of Ga, Zn, O, and Er were assessed by comparing the Ga $2p_{3/2}$, Zn $2p_{3/2}$, O $1s$ and Er $4d$ spectra of the samples (ZGO, ZGO+Er) with those of Ga_2O_3 (film, obtained by the method of halide vapor-phase epitaxy (HVPE)), ZnO (pressed powder, purity 99.99%), and Er_2O_3 (pressed powder, purity 99.99%) in terms of line shapes and binding energies. Survey and core-level spectra were obtained at analyzer pass energies of 100 and 50 eV and energy step sizes of 1 and 0.1 eV, respectively. Additionally, before XPS measurements, all samples were etched with argon ions at an energy of 3 keV for 60 s to remove surface contaminants (atoms and molecules from the atmosphere). The position of the C $1s$ peak maximum of saturated hydrocarbon contamination at 285.0 eV was used as an internal reference for calibration of each spectrum. The binding energy scale was calibrated using the Au $4f_{7/2}$ peak at 84.0 eV and the Fermi level measured on a pure gold foil. Data processing was conducted using the Casa XPS software (version 2.3.16).

To establish the elemental composition of the films, energy dispersive X-ray (EDX) spectroscopy was performed using an Axia ChemiSEM (Thermo Fisher Scientific, Waltham, MA, USA) scanning electron microscope equipped with an appropriate spectrometer at an accelerating voltage of 5 kV.

The surface microrelief of the samples was investigated using the high-resolution field emission scanning electron microscopy (HR FESEM) and atomic-force microscopy (AFM). HR FESEM was performed using an Apreo 2S microscope (Thermo Fisher Scientific, Waltham, MA, USA) at an accelerating voltage of 5 kV. To realize AFM, a Solver HV microscope (NT-MDT, Beijing, China) was used in semi-contact mode with a NSG30_SS (TipsNano, Beijing, China) cantilever at a rounding radius of 2 nm.

The diffuse reflectance spectra of the samples were measured using a Persee T8DCS (Beijing, China) dual-beam spectrophotometer with an integrating sphere.

Pt contacts were deposited on the samples' surface by means of magnetron sputtering through a shadow mask. The samples with the contacts were divided into separate samples with a size of ~5 mm $\times$ 5 mm. The interelectrode distance was 1.2 mm.

The gas sensing measurements of the samples were performed by means of a sealed chamber with a Nextron MPS-CHH microprobe station. The chamber volume was 100 cm^3. A ceramic-type heater, installed in the chamber, was used to heat the samples. The heater allowed T to be set and controlled in the range from RT to 750 °C with a T accuracy control of ±0.1 °C. The gas mixture of pure dry air + CH_4 was pumped through the measuring chamber. The pure dry air was generated using a special generator GPA-1,2-3,5 (Himelektronika LLC, Moskow, Russia) that produces air with a residual concentration of moisture and hydrocarbon contaminants of no more than 10 ppm and 0.1 ppm, respectively. The concentration of the CH_4 in the gas mixture was controlled by a gas mixing and a delivery system Microgas F-06 (MICROMED S.r.l., Roma, Italy) based on the Bronkhorst gas flow regulators. The total flow rate of the gas mixture through the measuring chamber was 1000 cm^3/min. The relative error of the gas mixture flow rate did not exceed 1.5%. Figure 1 shows a photo of the samples with Pt contacts in the measuring chamber.

Before starting the gas-sensitive properties studies, the samples were heated in a measuring chamber in a stream of pure dry air at T = 650 °C for 5 min to stabilize the Pt contact properties. The time dependences of the resistance of the samples were measured by means of a Keithley 2636A source-meter (TEKTRONIX, INC., Beaverton, OR, USA). The voltage applied to the sample's contacts during the measurements of time dependencies of the resistance was kept at 5 V.
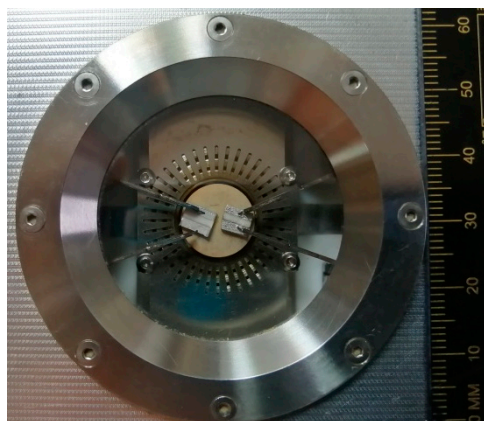
Figure 1. Photo of the samples in the measuring chamber.

The following ratio was chosen as the response *S* of the samples to CH_4:

$$S = R_{air}/R_g, \tag{1}$$

where R_{air} is the resistance of samples in pure dry air; R_g is the resistance of samples in a gas mixture of pure dry air + CH_4.

The time interval between the starting point of the interaction between gas mixture and samples, and the moment when sample resistance $R = 1.1 \times R_g$ was chosen as the response time t_{res} under exposure to CH_4. The time interval between the starting of pure dry air pumping through the measuring chamber and the moment when $R = 0.9 \times R_{air}$ was chosen as the recovery time t_{rec} after exposure to CH_4.

To investigate the impact of relative humidity *RH* on samples responses to CH_4 pure dry air was passed through a bubbler containing distilled water before entering a homogenizer where it was mixed with pure dry air and/or pure dry air + target gas mixture streams from other channels. By varying the flow ratios through the channels, the desired *RH* level in the measuring chamber was achieved. *RH* was measured using a HIH 4000 Honeywell capacitive sensor (Honeywell, Charlotte, NC, USA) with an absolute error of $\pm 3.5\%$.

In addition to CH_4 and high humidity, the samples were exposed to mixtures of pure dry air with H_2, CO, CO_2, NH_3, NO_2, NO, C_2H_4, C_3H_8, and C_4H_{10} to evaluate their selectivity to these habitat and industry-relevant gases. When investigating the samples' sensitivity to O_2, a pure N_2 atmosphere was chosen as the initial environment.

3. Results

3.1. Structural Properties

The XRD analysis (Figure 2) of the $ZnGa_2O_4$ (ZGO) sample revealed that the main crystalline phase is zinc digallium oxide ($ZnGa_2O_4$), identified as a cubic spinel structure belonging to the Fd-3m space group and referenced in ICDD 01-086-0415. This primary phase comprises 80.7% of the material, while the secondary phase, β-Ga_2O_3, accounts for 19.3% and is indexed as ICDD 00-041-1103. The lattice parameters for $ZnGa_2O_4$ were determined to be $a = b = c = 8.3279$ Å with a unit cell volume of 577.568 Å^3. D_c of $ZnGa_2O_4$ is 64.8 nm, with an associated ε of 0.066%. In contrast, the secondary β-Ga_2O_3 phase exhibited lattice parameters of $a = 12.2373$ Å, $b = 3.0429$ Å, $c = 5.8092$ Å, and $\beta = 103.83°$, with a smaller D_c of 46.4 nm and ε of 0.067%.
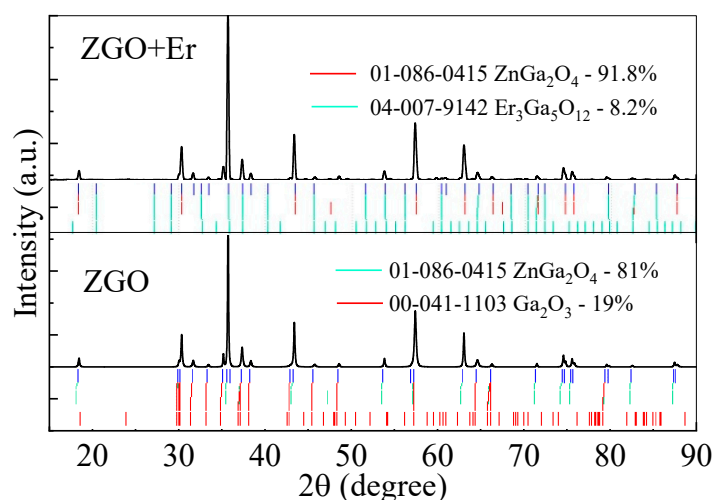
Figure 2. XRD spectra of ZGO and ZGO+Er samples.

In the Er-doped sample (ZGO+Er), the proportion of the primary $ZnGa_2O_4$ phase increased to 91.8%, with lattice parameters slightly expanded to a = 8.3331 Å and a unit cell volume of 578.66 Å^3. D_c of the $ZnGa_2O_4$ phase in this sample increased to 106.8 nm, while ε was slightly higher at 0.068%. The secondary phase in the ZGO+Er sample, triherbium pentagallium oxide ($Er_3Ga_5O_{12}$ or erbium gallium garnet), accounted for 8.2% of the composition and is referenced in ICDD 04-007-9142. This phase exhibited a cubic structure with lattice parameter a = 12.258 Å, a unit cell volume of 1841.8 Å^3, D_c of 50.5 nm, and ε of 0.072%.

The high degree of crystallinity in the $ZnGa_2O_4$ phase across both samples confirms the successful formation of polycrystalline $ZnGa_2O_4$ with a cubic spinel structure. The differences in phase composition and crystallite sizes between the pure and Er-doped samples indicate that the incorporation of erbium influences the structural and microstructural properties. The formation of the $Er_3Ga_5O_{12}$ phase suggests a partial interaction between Er_2O_3 and Ga_2O_3 during high-temperature annealing, as confirmed by the identification of phases using the ICDD database. These results demonstrate that both the ZGO and ZGO+Er samples possess desirable structural qualities, making them suitable for potential applications in optical and electronic technologies.

The chemical composition of the studied samples ZGO and ZGO+Er was determined based on a detailed analysis of the photoelectron lines of the corresponding elements from the survey PE spectra () taking into account the atomic sensitivity factors based on Scofield cross-sections (Table 2). The data in Table 2 show that both samples contain zinc, gallium, oxygen, and carbon. In the case of ZGO+Er, Er is also additionally present in an amount of 0.2 at.%. In general, it can be noted that the chemical composition of the samples is similar, and the presence of a small amount of carbon (about 3.5–3.8 at.%) is apparently associated with its introduction into the composition of the surface layers of the samples at the stage of their synthesis.

Table 2. Chemical composition of the surface region of ZGO and ZGO+Er samples by XPS.

Material	Concentration, at.%				
	[Zn]	**[Ga]**	**[O]**	**[Er]**	**[C]**
ZGO	12.1	31.8	52.3	-	3.8
ZGO + Er	11.9	31.5	52.9	0.2	3.5

Now, let us proceed to a detailed examination of the core-level (Ga $2p_{3/2}$, Zn $2p_{3/2}$, O $1s$, Er $4d$) PE spectra of both samples, starting with the Ga $2p_{3/2}$ spectra (Figure 3). It is clearly seen that the maximum of the Ga $2p_{3/2}$ spectrum in the ZGO sample is located at 1119.6 eV, which is +1.2 eV higher than for the reference sample Ga$_2$O$_3$. Such a high-energy shift is due to the fact that gallium is surrounded not only by oxygen, but also by zinc in the ZnGa$_2$O$_4$ compound. At the same time, a slight asymmetry of the line is observed on the side of low binding energies, which indicates the presence of a small amount of gallium also in Ga$_2$O$_3$. This result agrees well with the XRD data (Figure 2). When moving from the ZGO sample to the ZGO+Er sample, one can see a subsequent high-energy shift of the $2p_{3/2}$ spectrum by +0.9 eV, as well as the appearance of a clear intense shoulder on the side of low binding energies. Both results are due to the incorporation of erbium into the sample structure. Moreover, the largest amount of gallium in ZGO+Er is in the ZnGa$_2$O$_4$ compound, as in the ZGO sample, while some amount is in another compound. Considering that the position of the low-energy component in ZGO+Er is 0.4 eV higher than that of the similar component in the ZGO sample, and the fact that, according to the XRD data, Ga$_2$O$_3$ is absent in ZGO+Er, we can conclude that gallium is in a compound with erbium. Combining the data of XRD, EDX, and the information obtained from the analysis of diffuse reflectance spectra and the results of XPS, it can be assumed that the low-energy component in the spectrum of Ga $2p_{3/2}$ is associated with the Er$_3$Ga$_5$O$_{12}$ compound. It is interesting that similar energy shifts in the Zn $2p_{3/2}$ spectra are observed in the series ZnO → ZGO → ZGO+Er (Figure 3). However, two important features should be noted: the magnitudes of these shifts are smaller than in the case of Ga $2p_{3/2}$ spectra, and the fact that in both studied samples, the $2p_{3/2}$ zinc line is symmetrical. These results indicate, on the one hand, that zinc is in only one chemical state—in ZnGa$_2$O$_4$, and on the other hand, that additionally introduced erbium in ZGO+Er has a slightly smaller effect on the charge state of zinc compared to gallium. When analyzing the O $1s$ spectra (Figure 3), only small energy shifts can be seen, since the binding energies of the metal oxides used in this work differ insignificantly. Finally, the analysis of the Er $4d$ spectra allowed us to establish that erbium is present only in the ZGO+Er sample. Moreover, the shape of the spectrum in the studied sample and in the spectrum of the reference compound Er$_2$O$_3$ is close, which indicates the presence of erbium in Er^{3+}. At the same time, taking into account the shift of +1.1 eV of the Er $4d$ spectrum in the ZGO+Er sample relative to the Er$_2$O$_3$ spectrum and the conclusions made above when analyzing the Ga $2p_{3/2}$ spectrum, we can be confident that erbium is bonded with gallium and oxygen in the compound Er$_3$Ga$_5$O$_{12}$.
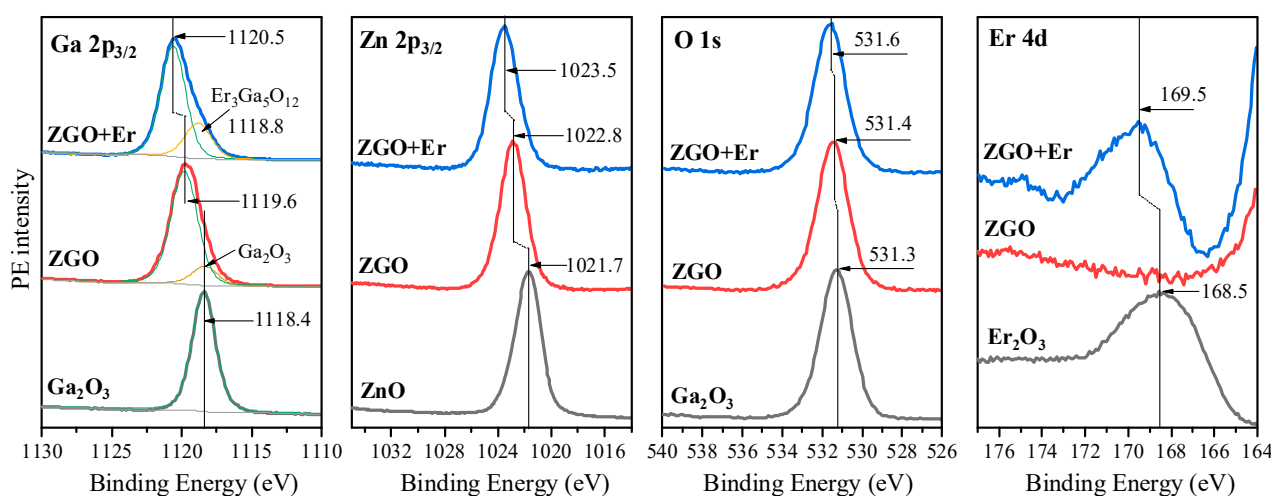

Figure 3. Ga $2p_{3/2}$, Zn $2p_{3/2}$, O $1s$, Er $4d$ spectra of ZGO and ZGO+Er samples as well as the reference compounds Ga$_2$O$_3$, ZnO and pure Er$_2$O$_3$.

The surface of ZGO samples is relatively smooth and characterized by the presence of pores extending to the surface (Figure 4a). The pore sizes on the surface of the samples vary from 8 μm to 17 μm. The addition of Er significantly changes the surface morphology of the samples (see Figure 4b). The SEM image of the ZGO+Er surface clearly distinguishes the microcrystals of two types, with different electron densities, and the interfaces between microcrystals of one and different types. Microcrystals of the first type have facets of regular geometric shapes characteristic of the cubic crystal lattice. The size of microcrystals of the first type varies in the range from 1 μm to 7 μm. Microcrystals of the second type, spherical in shape, are predominantly embedded in the structure of the samples and segregate on the surface. The size of microcrystals of the second type varies in the range from 0.5 μm to 4 μm. In addition, for ZGO+Er, the density of pores extending to the surface of the samples increases. The size of pores extending to the surface of ZGO+Er samples varies from 1 μm to 7 μm. According to the analysis of AFM images (Figure 5), the root mean square of the surface roughness of the samples increases from 787.8 nm to 895.5 nm with the addition of Er. ZGO+Er samples are characterized by a significantly larger active surface. The increased pore density and roughness of the ZGO+Er samples must contribute to the higher CH_4 response by enhancing gas adsorption. Also, on the surface of samples of both types, there are small clusters of the order of 10–100 nm, probably due to the residues of precursors that did not react during synthesis of the samples.
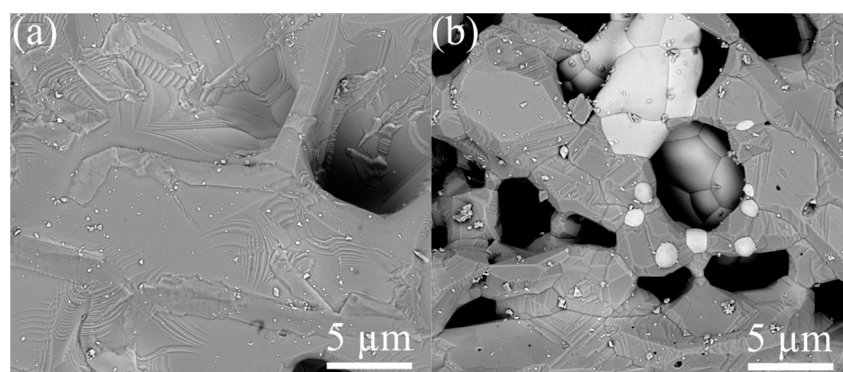

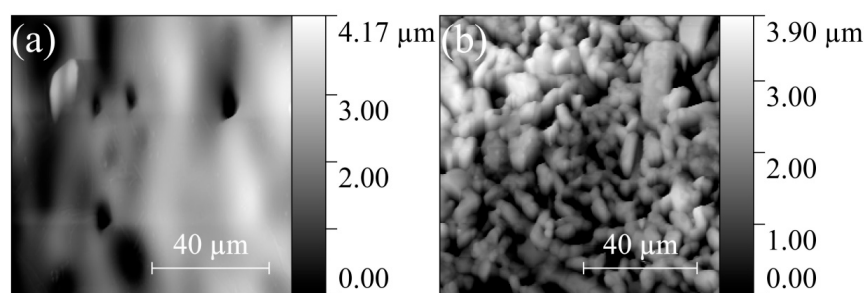**Figure 4.** SEM images of the ZGO (**a**) and ZGO+Er (**b**) surfaces.

Figure 5. AFM images of the ZGO (**a**) and ZGO+Er (**b**) surfaces.

There are difficulties in determining the concentration of constituent elements in the samples due to the overlap of Ga and Zn lines on the one hand, and the insulating properties of the samples at RT on the other hand. The EDX analysis of the ZGO samples did not reveal the presence of extrinsic elements other than Ga, Zn, and O, which are homogeneously distributed over the area. EDX analysis showed that the second-type microcrystals for ZGO+Er samples (Figure 6) are characterized by a high Er content. The concentration of Er in these microcrystals exceeds the concentrations of Ga and Zn. Based

on the XRD and EDX results, it can be assumed that microcrystals of the second type correspond to the superstoichiometric $Er_3Ga_{5-x}O_{12-y}$ phase.
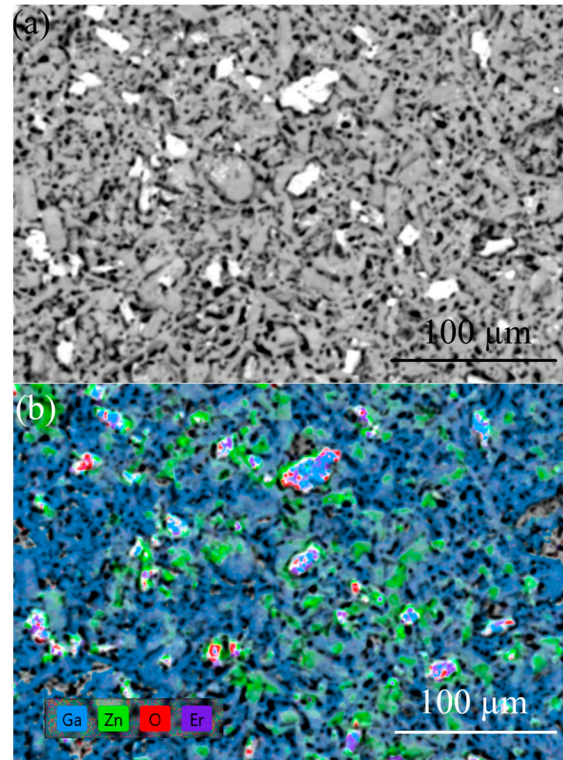

Figure 6. SEM image (**a**) and corresponding EDX mapping (**b**) of the ZGO+Er surface.

The diffuse reflectance spectrum of the ZGO sample is typical (Figure 7). Regardless of the chemical composition of the samples, a sharp absorption edge in the ultraviolet region is observed, which corresponds to intrinsic absorption in $ZnGa_2O_4$. The Kubelka–Munk estimates showed that the E_g of ZGO is 4.29 eV, which is in agreement with the literature data [63]. When Er_2O_3 is added into the ZGO composition, a slight decrease in the reflectance intensity in the absorption edge region is observed. This may be due to the introduction of defects or the state of levels inside the band gap of $ZnGa_2O_4$ due to the presence of Er^{3+} ions. Additional peaks appear on the reflection spectrum of the ZGO+Er sample in the wavelength range of 400–800 nm due to the appearance of additional energy levels in the band gap of $ZnGa_2O_4$, as well as partially coinciding with the absorption of the $Er_3Ga_5O_{12}$ phase. The spectrum typical of the ZGO+Er samples contains a set of narrow peaks characteristic of the internal 4f $\rightarrow$ f transitions of electrons in Er^{3+} ions, the positions of which are presented in Table 3.
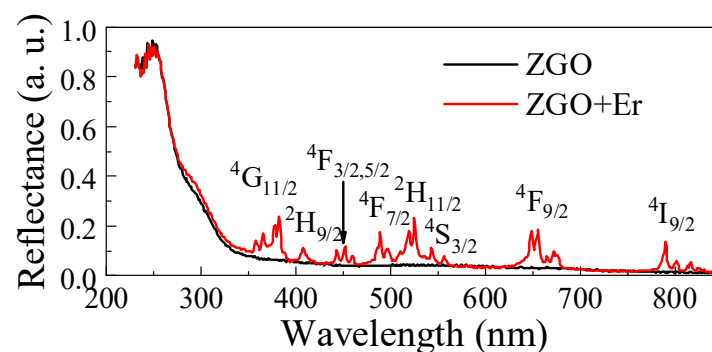

Figure 7. Reflection spectra of ZGO and ZGO+Er samples.

Table 3. Spectral lines of electron transitions in the Er^{3+} ion for ZGO+Er samples.

Transition from $^4I_{15/2}$	Spectral Interval (nm)
$^4G_{11/2}$	355.0–387.0
$^2H_{9/2}$	407.84
$^4F_{3/2, 5/2}$	438.0–463.0
$^4F_{7/2}$	476.2–506.0
$^2H_{11/2}$	504.0–530.0
$^4S_{3/2}$	538–564
$^4F_{9/2}$	630.0–683.0
$^4I_{9/2}$	781–842

3.2. Gas-Sensitive Properties

Figure 8 displays the temperature dependencies of the samples' basic resistance in dry air in Arrhenius coordinates, $\ln(R_{air})$ vs. $10^3/T_K$, where R_{air} is chosen as the basic resistance; T_K is the absolute temperature of the sample. At $T = 250\,°C$, R_{air} is high and reaches ~10^{12} Ohm. As the temperature increases, the R_{air} of the samples decreases according to the exponential law. Heating the samples up to $T > 650\,°C$ leads to an irreversible increase in R_{air}. For this reason, measurements of the gas-sensitive properties of the samples at $T > 650\,°C$ were not performed. The R_{air} of the ZGO samples with addition of Er decreases in 2.0–2.6 times in the whole T interval. Regardless of the chemical composition of the samples, two sections can be distinguished on the Arrhenius curves in the interval of $T = 250–650\,°C$, the first in the interval of $T = 250–350\,°C$, and the second–$T = 350–650\,°C$. The first section is characterized by the activation energy ΔE_1, and the second—by ΔE_2. For ZGO samples, $\Delta E_1 = 0.68 \pm 0.08$ eV and $\Delta E_2 = 1.56 \pm 0.02$ eV. For ZGO+Er samples, $\Delta E_1 = 0.7 \pm 0.1$ eV and $\Delta E_2 = 1.52 \pm 0.04$ eV. The addition of Er has no effect on the position of the levels associated with ΔE_1 and ΔE_2, which are due to the presence of defects in ZGO, including antisite defects [64].
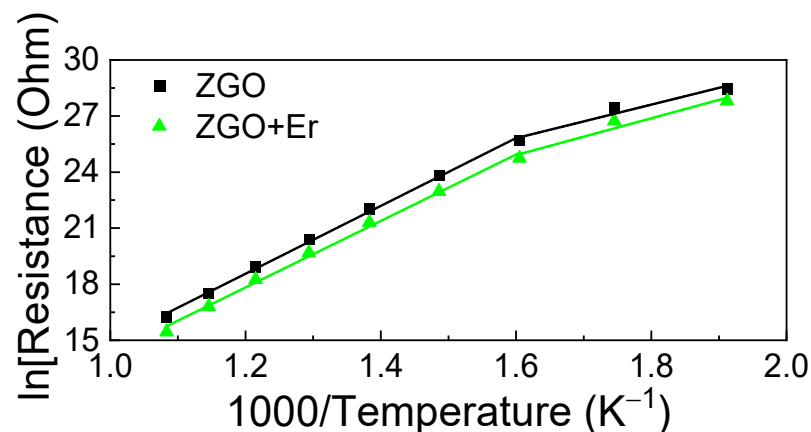
Figure 8. Dependence of the sample's basic resistance in ln scale on the inverse absolute temperature.

For ZGO, it was possible to register the response to CH_4 in the range of $T = 550–650\,°C$ (Figure 9). These samples are characterized by weak responses to CH_4. The maximum response S_{max} at $T = 650\,°C$ and under exposure to 10^4 ppm of CH_4 is only 1.33 a.u. The addition of Er allows one to significantly increase the response of samples to CH_4 and to extend the range of T, at which the samples show sensitivity to gas, to the low temperature region. S_{max} for ZGO+Er at $T = 650\,°C$ and exposure to 10^4 ppm of CH_4 is 14.77 a.u. At the same time, the base resistivity of the samples with addition of Er decreased only by a factor of 2. Due to the high sensitivity of ZGO+Er samples to CH_4, we will further focus on their gas-sensitive properties.
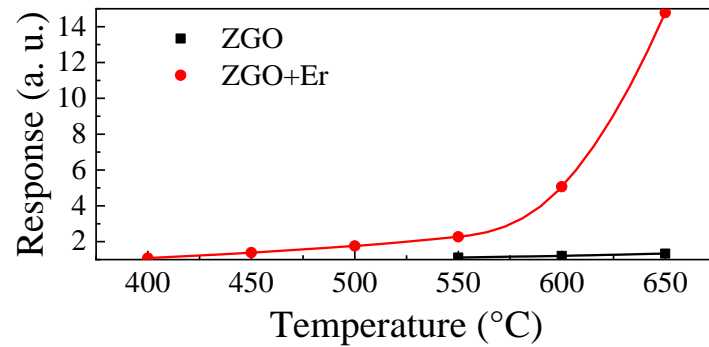
Figure 9. Temperature dependencies of the ZGO and ZGO+Er responses to 10^4 ppm of CH_4.

The dependences of the responses of ZGO+Er to CH_4 on concentration n_g were measured in the range of Δn_g = 100–20,000 ppm and at T = 650 °C (Figure 10). The samples exhibited responses at all gas concentrations in Δn_g. The response increases with n_g according to a power law, S $\sim n_g{}^m$, where m is the power index. At T = 650 °C for ZGO+Er samples $m = 0.48 \pm 0.01$. It can be seen that the response does not reach saturation at high $n_g = (1-2) \times 10^4$ ppm. Also, the S to 100 ppm of CH_4 is 2.91 a. u. The dynamic range Δn_g of the investigated samples can be extended to both high and low n_g regions. Setting n_g below 100 ppm is limited by the capabilities of the involved equipment, and above 2×10^4 ppm by safety requirements.
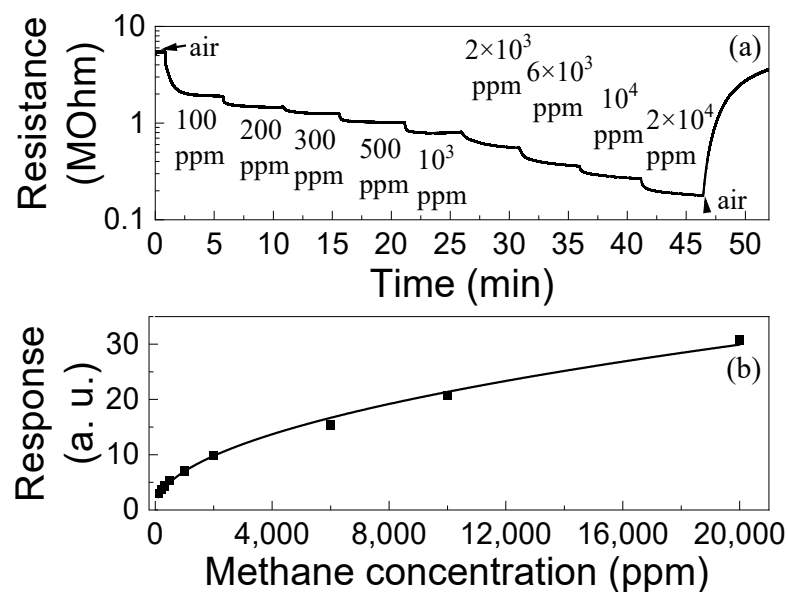

Figure 10. Time dependence of the ZGO+Er samples resistance at T = 650 °C and exposure to different concentrations of CH_4 (**a**); Dependence of the ZGO+Er samples response at T = 650 °C on CH_4 concentration (**b**).

The time dependences of the resistance of the ZGO+Er samples at T = 650 °C and the cyclic exposure to 2000 ppm of CH_4, illustrated in Figure 11a, were used to evaluate the speed-performance and stability of gas-sensitive characteristics in short-term tests. The t_{res} of the samples at the first gas exposure was 90 s. For 5 min after gas exposure, the resistance of the specimens did not recover to the R_{air} level. Probably, such long response and recovery times of the specimens are due to the large active surface (Figures 4 and 5). The sections of

the samples' resistance decrease under CH_4 exposure and of resistance growth after CH_4 exposure are approximated by the following exponential functions, respectively:

$$R(t) = R_g{}^{st} + A \times \exp(-t/\tau_1), \tag{2}$$

$$R(t) = R_{air}{}^{st} - B \times \exp(-t/\tau_2), \tag{3}$$

where $R_g{}^{st}$ is the steady-state value of the sample resistance in the gas mixture of pure dry air + 2000 ppm of CH_4; $R_{air}{}^{st}$ is the steady-state value of the sample resistance in pure dry air; A and B are constants; τ_1 and τ_2 are time constants. For the second cycle of gas exposure, $\tau_1 = 9$ s and $\tau_2 = 197$ s. $\tau_1 << \tau_2$ is satisfied under exposure to CH_4 at all operating temperatures and n_g.
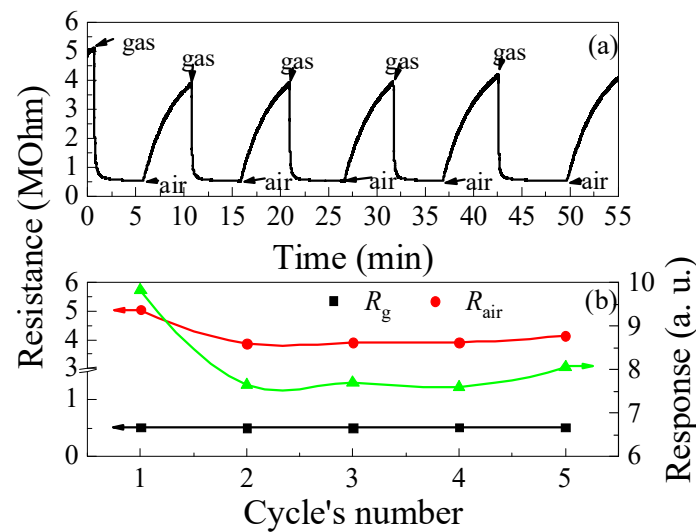

Figure 11. Time dependence of the ZGO+Er samples resistance at $T = 650\ °C$ and cyclic exposure to 2000 ppm of CH_4—(**a**); Variations of the base resistance, resistance in the gas mixture of pure dry air + 2000 ppm of CH_4 and response to 2000 ppm of CH_4 under cyclic gas exposure—(**b**).

After the first cycle of CH_4 exposure, the response of the samples drops by a factor of 1.28, mainly due to the decrease in R_{air} caused by the prolonged recovery of the sample's resistance (see Figure 11b). It is worth noting that R_g under the above conditions is practically unchanged and varies in the range of $(5.06–5.14) \times 10^5$ Ohm.

Increasing the humidity of the gas–air mixture leads to a decrease in the sample's response to CH_4, as exhibited in Figure 12. The response of samples decreases significantly by 46% when the *RH* increases from 0 to 30% (Figure 12b). Increasing the *RH* from 0 to 30% results in an increase in R_g by a factor of about 2.13, while R_{air} increases by only a factor of 1.14 (Figure 12a). The decrease in the response to CH_4 with increasing *RH* is due to the large-scale increase in R_g. It is worth noting that, in the range of $RH = 30–70\%$, the response to CH_4 is practically independent of humidity.

The results of long-term studies of changes in the gas-sensitive characteristics of the samples for 19 days are depicted in Figure 13. Obviously, there is a tendency for R_g, R_{air}, and S to increase with the duration of the tests. The samples were stored in hermetically sealed packaging at RT between measurements, and for the long-term tests, as-prepared fresh samples were used, which had not been previously heated to high temperatures and exposed to gases. During 19 days of tests, the R_g, R_{air}, and response to 2000 ppm of CH_4 for ZGO+Er samples increased by 1.2, 1.4, and 1.26 times, respectively. At the same time, non-symbatic changes in R_g and R_{air} were observed from test to test, which was reflected in the non-monotonic variation of response values with test duration. The response value

achieved on the 19th day of testing for the as-prepared samples is comparable to the response values for aged samples tested under heating to different temperatures and exposure to different gases (see Figures 8–12).
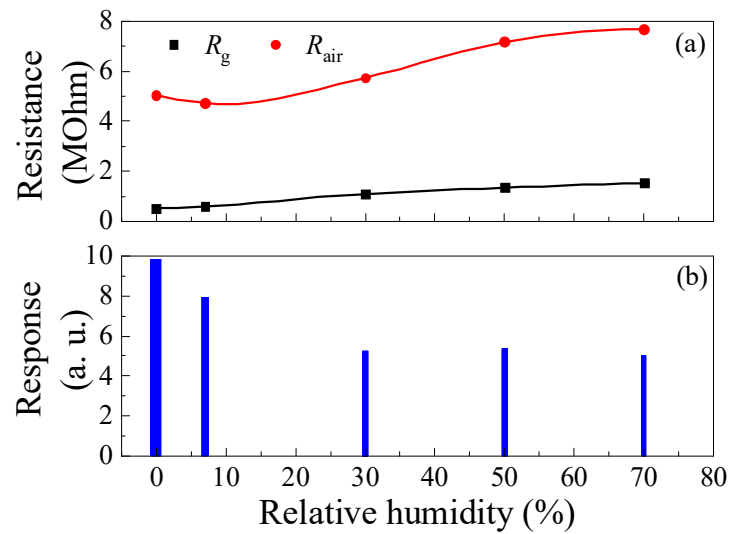

Figure 12. Effect of humidity on ZGO+Er samples' base resistance, resistance in the gas mixture of pure dry air + 2000 ppm of CH_4 (**a**) and response to 2000 ppm CH_4 (**b**) at $T = 650\ °C$.
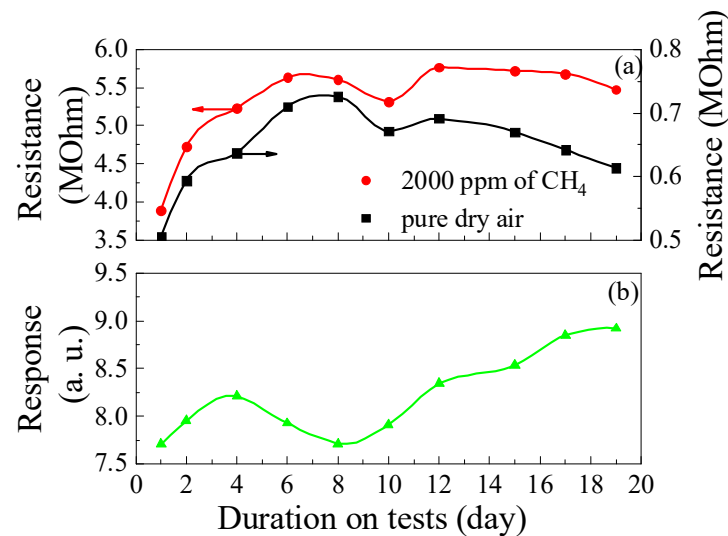

Figure 13. Long-term test results: Changes in the ZGO+Er samples base resistance and resistance in the gas mixture pure dry air + 2000 ppm of CH_4 (**a**); Changes in the ZGO+Er samples' response to 2000 ppm of CH_4 (**b**) at $T = 650\ °C$.

The results of the selectivity evaluation for the ZGO+Er samples at $T = 650\ °C$ are shown in Figure 14. The resistance of the samples dropped under exposure to H_2, CO, CO_2, NH_3, and hydrocarbons, while the resistance of the samples increased under exposure to NO_2 and O_2. The ratios of the ZGO+Er samples' responses to other gases and CH_4 at same gas concentration of 100 ppm are presented in Table 4. As can be seen, the responses to NO_2, H_2, and hydrocarbons outperform those to CH_4. The samples showed a particularly high response when exposed to hydrocarbons (C_2H_4, C_3H_8 and C_4H_{10}). A noticeable response to NH_3 was also obtained. For the remaining gases CO, CO_2, and O_2, the responses were low. The response to 5 ppm of NO was 1.22 a.u.
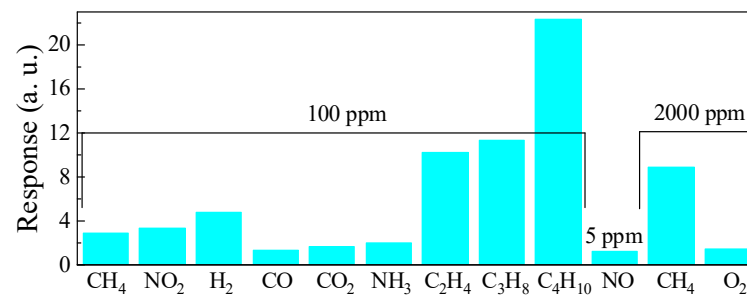
Figure 14. Comparison of the ZGO+Er samples responses to different gases at $T = 650\ ^\circ$C.

Table 4. Ratios of the ZGO+Er samples responses to 100 ppm CH_4 and other gases.

| Gas	Response Ratio at 100 ppm
NO_2	1.16
H_2	1.64
CO	0.47
CO_2	0.58
NH_3	0.71
C_2H_4	2.41
C_3H_8	2.75
C_4H_{10}	3.09

4. Discussion

ZGO+Er samples do not exhibit exceptional selectivity to CH_4 in contrast to the $ZnGa_2O_4$-based samples presented in Refs. [11,12,22,37–41], where exceptionally high responses to NO_x or LPG were obtained. It is worth noting that the samples are more sensitive to NO_2 and LPG components (C_3H_8 and C_4H_{10}) (see Figure 14 and Table 4). Exceptional selectivity is not characteristic for MOS gas sensors [65]. Generally, these materials show sensitivity to many gases, but to varying degrees depending on many factors such as temperature, humidity, etc. [65]. This is due to the sensing effect of MOSs. In the air atmosphere, oxygen chemisorbs on the surface of semiconductors capturing electrons. This process for *n*-type semiconductors leads to the appearance of the layer depleted of electrons at the pre-surface region and the energy bands bending upward. When CH_4 appears, there is an interaction between its molecules and oxygen ions chemisorbed on the semiconductor surface, leading to a decrease in the surface density of the latter and the return of electrons to the semiconductor.

For polycrystalline semiconductors with large microcrystals, as in our case, the conditions at the microcrystal boundary influence the charge carrier transport [58]. For such semiconductors, the resistance in the air is described by the following formula [66]:

$$R_{\text{air}} = R_0 \times \exp[(e\varphi_{\text{s}}/(kT_{\text{K}})], \tag{4}$$

where R_0 is a value determined by the geometric and electrophysical parameters of the sample; $e\varphi_{\text{s}}$ is the energy bands bending at the microcrystal boundary; e is the electron charge; φ_{s} is the surface potential in air; and k is the Boltzmann constant. R_0 weakly depends on changes in the atmospheric composition. $e\varphi_{\text{s}} \sim N_{\text{i}}^2/N_{\text{d}}$ and $N_{\text{i}} \sim n_{\text{ox}}^l$, where N_{i} is the surface density of chemisorbed oxygen ions; N_{d} is the donor concentration; n_{ox} is the oxygen concentration; $l < 1$ [66,67]. $n_{\text{ox}} = \text{const}$ and N_{i} changes in pure dry air are due to changes in sample temperature and ambient humidity under experimental conditions [66,67]. For binary MOSs, analysis of data [68] obtained by electron paramagnetic resonance spectroscopy and temperature programmed desorption, as well as extensive

first-principles analysis [69], indicates that oxygen is chemisorbed in the form of O^{2-} at high temperatures. Based on these findings, we believe that a similar situation exists for the studied samples. The interaction of CH_4 and O^{2-} molecules may occur in two stages at $T = 650\ °C$ [58,59]:

$$CH_4 \rightarrow CH_3 + H, \tag{5}$$

$$CH_3 + H + 4O^{2-} \rightarrow CO_2 + 2H_2O + 8e^-. \tag{6}$$
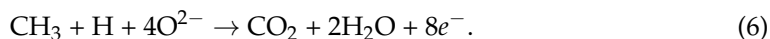
At the first stage, the dissociative adsorption of CH_4 molecules occurs with the appearance of $CH_3 + H$ fragments on the semiconductor surface, which interact with O^{2-} ions to form CO_2, H_2O molecules and free electrons, which are returned to the semiconductor. As a result of reaction (6), N_i is reversibly reduced, leading to a decrease in $e\varphi_s$ and the resistance of the semiconductor. The reaction products of CO_2 and H_2O are desorbed from the semiconductor surface.

Doping $ZnGa_2O_4$ with Er leads to lattice expansion, crystallite growth, and the formation of high-electron-density microcrystals. This is primarily due to the substitution of Ga^{3+} (0.62 Å) and Zn^{2+} (0.60 Å) with the larger Er^{3+} ion (0.89 Å), increasing the unit cell parameter from 8.3279 Å to 8.3331 Å and its volume from 577.568 $Å^3$ to 578.66 $Å^3$. The process induces point defects, such as oxygen vacancies, which further expand the lattice and slightly increase strain from 0.066% to 0.068%. Phase composition changes as β-Ga_2O_3 (19.3%) is replaced by $Er_3Ga_5O_{12}$ (8.2%), indicating gallium redistribution. The crystallite size of $ZnGa_2O_4$ grows from 64.8 nm to 106.8 nm, facilitated by Er^{3+} promoting grain growth and reducing structural defects. The newly formed $Er_3Ga_5O_{12}$ phase has a large unit cell (12.258 Å, 1841.8 $Å^3$) and contributes to increased electron density. These structural modifications enhance optical and electronic properties, making Er-doped $ZnGa_2O_4$ promising for luminescent and optoelectronic applications.

According to the results of SEM and AFM (Figures 4 and 5), the addition of Er leads to the formation of a larger active surface, represented by two types of microcrystals with characteristic sizes of 1–7 μm and 0.5–4 μm, respectively. At the same time, the base resistance of the samples (Figure 8) (resistance in pure air) decreases only by a factor of 2.0–2.6, and the response of the samples to CH_4 increases by a factor of 11.1 (Figure 9). The gas-sensing, electrical-conductivity, and other properties of $Er_3Ga_5O_{12}$ remain unexplored. Therefore, the proposal of a mechanism for increasing the response to gas based on the formation of a new phase of $Er_3Ga_5O_{12}$ is not justified. It has been shown that $Er_3Ga_5O_{12}$ demonstrates unique magnetic [70] and phosphor [71] properties, and is also used as a catalyst support for the Ni catalyst for CH_4 decomposition at $T = 650\ °C$ [72]. It is noted that $Er_3Ga_5O_{12}$ provides the most intense CH_4 decomposition. The temperature of use of the $Ni/Er_3Ga_5O_{12}$ catalyst coincides with the temperature of the maximum response of ZGO+Er to CH_4. However, the results of our research only allow us to conclude that the increase in the $ZnGa_2O_4$ response with Er addition is due to an increase in the material's active surface area (Figures 4 and 5). This, in turn, contributes to an increase in the surface density of adsorption centers for O^{2-}, which leads to an increase in the response to reducing gases [66]. A similar case was observed when Er was added to SnO_2 [56,73].

The temperature dependence of the response of MOS sensors (Figure 9) is determined by the processes that take place on the surface of the semiconductor and in the near-surface region of the semiconductor [74]. These processes are usually of an activation nature. Such processes are the physical adsorption and chemisorption of oxygen molecules, dissociative chemisorption of oxygen molecules, oxygen desorption, dissociative adsorption of methane molecules, desorption of interaction products of chemisorbed oxygen, and fragments of methane molecules, etc. Models have been developed to account for these processes, which are in agreement with experimental results [75]. In our case, the monotonous increase

in response with increasing temperature can be explained by an increase in the surface density of O^{2-} and an intensification of the dissociation of CH_4 molecules, facilitated by an additive containing Er.

An increase in the base resistance of *n*-type MOSs is not typical when humidity increases. During chemisorption at high temperatures, water molecules exhibit reducing gas properties and the effect should be reversed [67]. Further research is needed to explain the dependence of R_{air} on *RH*. An increase in R_g with an increase in *RH* can be explained by H_2O and CH_4 molecules competing for adsorption centers S_a. In an atmosphere of moist pure air, the following reaction takes place [76]:

$$H_2O + O^{2-} + S_a \rightarrow 2(S_a\text{–}OH) + 2e^-. \tag{7}$$
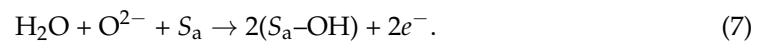
According to reaction (7), the semiconductor surface is poisoned by OH-groups, leading to a decrease in the surface density of S_a and N_i. As *RH* increases, fewer CH_4 molecules are chemisorbed onto the semiconductor surface, while R_g increases and *S* decreases.

To minimize the impact of humidity on the gas-sensitive properties of the samples, it is sensible to use the ultrathin films of materials that can absorb H_2O molecules and are deposited on the surface of the sensitive layer. One such material is SiO_2 [76]. It is worth noting that this material can withstand high-temperature operating conditions, which is important for developing appropriate high-temperature gas sensors [77]. To further reduce the effect of humidity, operating modes involving the modulation of the operating temperature and/or exposure to ultraviolet radiation are advisable [78].

According to refs. [66,67], $S \sim \exp(e\varphi_s)$. The mechanisms of the gas-sensitive characteristic drift of MOSs gas sensors are considered in ref. [79]. Operating sensors at high temperatures and under the exposure to CH_4 over a long period can cause structural transformations, changes in microcrystal size, and the poisoning of the sample surface. As a result of these processes, N_i can change. Other processes, such as phase transformations, the formation of electrically active defects, and bulk diffusion, primarily result in a change in N_d. According to our results (Figure 13), an increase in base resistance and response to CH_4 indicates an increase in the N_i^2/N_d over the duration of the tests. We believe that, as the test duration increases further, the characteristics will continue to stabilize, as is typical for MOSs gas sensors [79].

The authors are not aware of any publications devoted to the research and development of CH_4 sensors based on $ZnGa_2O_4$. To date, CH_4 sensors based on binary metal-oxide films and nanostructures (SnO_2, ZnO and TiO_2, primary) have been researched and developed [58–62]. The achieved response to CH_4 for ZGO+Er samples exceed the response for most sensors based on the binary MOSs presented. However, ZGO+Er samples are characterized by a high operating temperature, which, on the one hand, can lead to an increase in the power consumption of sensors, and on the other hand—the ability of sensors to function at elevated temperatures is of interest for a number of practical applications where the majority of the binary MOSs are not able to function reliably. High-temperature CH_4 sensors are of interest for the development of systems based on them for the monitoring and control of combustion processes, and for determining the ideal fuel/air mixture [3]. With this in mind, it is reasonable to compare the gas-sensitive characteristics of CH_4 sensors based on MOSs capable of functioning in the high-temperature region corresponding to the range of $T = 600$–$1000\ °C$. In addition, high operating temperatures ensure high sensor speed performance [80], low base resistance, and surface regeneration [79]. Table 5 shows a comparison of the gas-sensitive characteristics of high-temperature CH_4 sensors based on MOSs. The responses of ZGO+Er samples to equal CH_4 concentrations are significantly higher than those of thin Ga_2O_3 films with the addition of 0.1 at.% of SnO_2 and thick

$LaFe_{0.95}W_{0.05}O_3$ films. In Ref. [6], sensors based on polycrystalline Ga_2O_3 thin films with responses exceeding those of ZGO+Er were presented. However, such high responses were obtained at a higher *T*, at which we did not measure the characteristics of ZGO+Er samples due to the manifestation of characteristic drift. In addition, the authors explain the high responses for CH_4 by the partial combustion of the gas with the formation of ionized oxygen defects [6].

Table 5. Gas-sensitive characteristics of high-temperature CH_4 sensors based on MOSs.

Material	CH_4 Concentration (ppm)	Temperature (°C)	Response (a.u.)	Refs.
Ga_2O_3 with addition of 0.1 at.% SnO_2	10^4	740	10	[7]
Ga_2O_3	5000	740	~80	[6]
$LaFe_{0.95}W_{0.05}O_3$	10^4	650	~8	[8]
ZGO+Er	100 10^4	650	2.91 20.74	This work

5. Conclusions

Pure $ZnGa_2O_4$ and $ZnGa_2O_4$ with Er addition ceramic pellets were synthesized. For the first time, the gas sensitivity of $ZnGa_2O_4$ with Er addition ceramic pellets has been studied. The addition of Er leads to the formation of the $Er_3Ga_5O_{12}$ phase in the $ZnGa_2O_4$ host, more importantly to the formation of a larger active surface and allows an 11.1-fold increase in the response of $ZnGa_2O_4$ to CH_4. The samples were characterized by a wide dynamic range of CH_4 concentrations, 100–20,000 ppm, the weak dependence of gas-sensitive characteristics on relative humidity in the range of 30–70%, the weak changes of gas-sensitive characteristics under cyclic gas exposure, and the stabilization of characteristics for long-term tests. They also exhibited high responses to C_2H_4, C_3H_8, C_4H_{10}, NO_2, and H_2. A possible mechanism of the sensing effect of $ZnGa_2O_4$ with Er addition was proposed. It was suggested that the increase in gas responses with Er addition is due to the formation of a larger active surface. Therefore, $ZnGa_2O_4$ with Er addition is very prospective for the development of high-temperature hydrocarbon sensors for systems monitoring and controlling combustion processes and for determination of the ideal fuel/air mixture. Our future work will focus on optimizing the gas-sensitive properties of high-temperature hydrocarbons sensors based on $ZnGa_2O_4$ with Er addition ceramic pellets with the aim of increasing their gas sensitivity, decreasing the effect of on relative humidity in the range of 0–30%, and improving their selectivity under extreme operating conditions.

Institutional Review Board Statement: Not applicable.

Informed Consent Statement: Not applicable.

Data Availability Statement: The raw data supporting the conclusions of this article will be made available by the authors upon request.

Conflicts of Interest: Author Aleksei V. Almaev was employed by the company Fokon LLC. The remaining authors declare that the research was conducted in the absence of any commercial or financial relationships that could be construed as a potential conflict of interest.

References

1. Aldhafeeri, T.; Tran, M.K.; Vrolyk, R.; Pope, M.; Fowler, M. A Review of Methane Gas Detection Sensors: Recent Developments and Future Perspectives. *Inventions* **2020**, *5*, 28. [CrossRef]

2. Gautam, Y.K.; Sharma, K.; Tyagi, S.; Ambedkar, A.K.; Chaudhary, M.; Pal Singh, B. Nanostructured metal oxide semiconductor-based sensors for greenhouse gas detection: Progress and challenges. *R. Soc. Open Sci.* **2021**, *8*, 201324. [CrossRef] [PubMed]

3. Liu, Y.; Parisi, J.; Sun, X.; Lei, Y. Solid-state gas sensors for high temperature applications—A review. *J. Mater. Chem. A* **2014**, *2*, 9919–9943. [CrossRef]

4. Ghosh, A.; Zhang, C.; Shi, S.Q.; Zhang, H. High-Temperature Gas Sensors for Harsh Environment Applications: A Review. *Clean—Soil Air Water* **2019**, *47*, 1800491. [CrossRef]

5. Wu, H.; Zhong, S.; Bin, Y.; Jiang, X.; Cui, H. Ni-decorated WS_2-WSe_2 heterostructure as a novel sensing candidate upon C_2H_2 and C_2H_4 in oil-filled transformers: A first-principles investigation. *Mol. Phys.* **2025**, e2492391. [CrossRef]

6. Fleischer, M.; Meixner, H. A Selective CH_4 Sensor Using Semiconducting Ga_2O_3 Thin Films Based on Temperature Switching of Multigas Reactions. *Sens. Actuators B Chem.* **1995**, *25*, 544–547. [CrossRef]

7. Frank, J.; Fleischer, M.; Meixner, H.; Feltz, A. Enhancement of Sensitivity and Conductivity of Semiconducting Ga_2O_3 Gas Sensors by Doping with SnO_2. *Sens. Actuators B Chem.* **1998**, *49*, 110–114. [CrossRef]

8. Moseley, P.T.; Oprea, A.; Merdrignac-Conanec, O.; Kerlau, M.; Bârsan, N.; Weimar, U. Limitations on the Use of Perovskite-Structure Oxides in Gas Sensing as a Result of the Concurrent Operation of Separate Mechanisms. *Sens. Actuators B Chem.* **2008**, *133*, 543–546. [CrossRef]

9. Chikoidze, E.; Sartel, C.; Madaci, I.; Mohamed, H.; Vilar, C.; Ballesteros, B.; Belarre, F.; Corro, E.; Vales-Castro, P.; Sauthier, G.; et al. p-Type Ultrawide-Band-Gap Spinel $ZnGa_2O_4$: New Perspectives for Energy Electronics. *Cryst. Growth Des.* **2020**, *20*, 2535–2546. [CrossRef]

10. Byun, H.J.; Kim, J.U.; Yang, H. Blue, Green, and Red Emission from Undoped and Doped $ZnGa_2O_4$ Colloidal Nanocrystals. *Nanotechnology* **2009**, *20*, 495602. [CrossRef]

11. Wu, M.R.; Li, W.Z.; Tung, C.Y.; Huang, C.Y.; Chiang, Y.H.; Liu, P.L.; Horng, R.H. NO Gas Sensor Based on $ZnGa_2O_4$ Epilayer Grown by Metalorganic Chemical Vapor Deposition. *Sci. Rep.* **2019**, *9*, 7459. [CrossRef] [PubMed]

12. Chen, C.; Li, G.; Liu, Y. Synthesis of $ZnGa_2O_4$ Assisted by High-Energy Ball Milling and Its Gas-Sensing Characteristics. *Powder Technol.* **2015**, *281*, 7–11. [CrossRef]

13. Mushtaq, U.; Ayoub, I.; Yagoub, M.Y.A.; Shivaramu, N.J.; Coetsee, E.; Swart, H.C.; Kumar, V. Effect of Li^+ monovalent ion on the structural and optical properties of Dy^{3+} doped $ZnGa_2O_4$ phosphor. *Appl. Phys. A* **2024**, *130*, 494. [CrossRef]

14. Wang, B.; Wang, H.; Tu, B.; Zheng, K.; Gu, H.; Wang, W.; Fu, Z. Optical transmission, dispersion, and transition behavior of $ZnGa_2O_4$ transparent ceramic. *J. Am. Ceram. Soc.* **2023**, *106*, 1230–1239. [CrossRef]

15. Kawazoe, H.; Ueda, K. Transparent Conducting Oxides Based on the Spinel Structure. *J. Am. Ceram. Soc.* **1999**, *82*, 3330–3336. [CrossRef]

16. Safeera, T.A.; Khanal, R.; Medvedeva, J.E.; Martinez, A.I.; Vinitha, G.; Anila, E.I. Low Temperature Synthesis and Characterization of Zinc Gallate Quantum Dots for Optoelectronic Applications. *J. Alloys Compd.* **2018**, *740*, 567–573. [CrossRef]

17. Reshmi, R.; Krishna, K.M.; Manoj, R.; Jayaraj, M.K. Pulsed Laser Deposition of $ZnGa_2O_4$ Phosphor Films. *Surf. Coat. Technol.* **2005**, *198*, 345–349. [CrossRef]

18. Han, D.; Liu, K.; Hou, Q.; Chen, X.; Yang, J.; Li, B.; Zhang, Z.; Liu, L.; Shen, D. Self-Powered Solar-Blind $ZnGa_2O_4$ UV Photodetector with Ultra-Fast Response Speed. *Sens. Actuators A Phys.* **2020**, *315*, 112354. [CrossRef]

19. Lin, W.; Zhang, D.; Liu, S.; Li, Y.; Zheng, W.; Huang, F. ZnGa$_2$O$_4$ Deep-Ultraviolet Photodetector Based on Si Substrate. *Mater. Lett.* **2021**, *283*, 128805. [CrossRef]

20. Cheng, L.C.; Huang, C.Y.; Horng, R.H. Thickness Effect on Operational Modes of ZnGa$_2$O$_4$ MOSFETs. *IEEE J. Electron Devices Soc.* **2018**, *6*, 432–437. [CrossRef]

21. Shen, Y.S.; Wang, W.K.; Horng, R.H. Characterizations of Metal-Oxide-Semiconductor Field-Effect Transistors of ZnGaO Grown on Sapphire Substrate. *IEEE J. Electron Devices Soc.* **2017**, *5*, 112–116. [CrossRef]

22. An, S.; Park, S.; Ko, H.; Jin, C.; Lee, C. NO$_2$ Gas Sensing Properties of Multiple Networked ZnGa$_2$O$_4$ Nanorods Coated with TiO$_2$. *J. Nanosci. Nanotechnol.* **2015**, *15*, 433–438. [CrossRef] [PubMed]

23. Pathania, A.; Dhanda, N.; Verma, R.; Sun, A.C.A.; Thakur, P.; Thakur, A. Review—Metal Oxide Chemoresistive Gas Sensing Mechanism, Parameters, and Applications. *ECS Sens. Plus* **2024**, *3*, 013401. [CrossRef]

24. Bulowski, W.; Knura, R.; Socha, R.P.; Basiura, M.; Skibińska, K.; Wojnicki, M. Thin Film Semiconductor Metal Oxide Oxygen Sensors: Limitations, Challenges, and Future Progress. *Electronics* **2024**, *13*, 3409. [CrossRef]

25. Zhai, H.; Wu, Z.; Fang, Z. Recent Progress of Ga$_2$O$_3$-Based Gas Sensors. *Ceram. Int.* **2022**, *48*, 24213–24233. [CrossRef]

26. Almaev, A.V.; Yakovlev, N.N.; Erzakova, N.N.; Mochalov, L.A.; Kudryashov, M.A.; Kudryashova, Y.P.; Nesov, S.N. Gas Sensitivity of PECVD β-Ga$_2$O$_3$ Films with Large Active Surface. *Mater. Chem. Phys.* **2024**, *320*, 129430. [CrossRef]

27. Almaev, A.V.; Yakovlev, N.N.; Verkholetov, M.G.; Rudakov, G.A.; Litvinova, K.I. High Oxygen Sensitivity of TiO$_2$ Thin Films Deposited by ALD. *Micromachines* **2023**, *14*, 1875. [CrossRef]

28. Almaev, A.; Yakovlev, N.; Kopyev, V.; Nikolaev, V.; Butenko, P.; Deng, J.; Pechnikov, A.; Korusenko, P.; Koroleva, A.; Zhizhin, E. High Sensitivity Low-Temperature Hydrogen Sensors Based on SnO$_2$/κ(ε)-Ga$_2$O$_3$:Sn Heterostructure. *Chemosensors* **2023**, *11*, 325. [CrossRef]

29. Dimitrova, Z.; Gogova, D. On the Structure, Stress and Optical Properties of CVD Tungsten Oxide Films. *Mater. Res. Bull.* **2005**, *40*, 333–340. [CrossRef]

30. Yurchenko, O.; Diehle, P.; Altmann, F.; Schmitt, K.; Wöllenstein, J. Co$_3$O$_4$-Based Materials as Potential Catalysts for Methane Detection in Catalytic Gas Sensors. *Sensors* **2024**, *24*, 2599. [CrossRef]

31. Zhan, H.; Li, H.; Yang, X.; Zhao, R.; Liu, Q.; Duan, Y.; Shen, Z. Pt-functionalized ZnO nanosheets gas sensor for highly sensitive detecting of methane. *J. Mater. Sci. Mater. Electron.* **2024**, *35*, 1871. [CrossRef]

32. Furuta, D.; Sayahi, T.; Li, J.; Wilson, B.; Presto, A.A.; Li, J. Characterization of inexpensive metal oxide sensor performance for trace methane detection. *Atmos. Meas. Tech.* **2022**, *15*, 5117–5128. [CrossRef]

33. Shaposhnik, A.V.; Moskalev, P.V.; Arefieva, O.A.; Zvyagin, A.A.; Kul, O.V.; Vasiliev, A.A. Selective determination of hydrogen in a mixture with methane using a single metal oxide sensor. *Int. J. Hydrogen Energy* **2024**, *82*, 523–530. [CrossRef]

34. Yablokov, M.Y.; Vasiliev, A.A.; Gainutdinov, R.V.; Sokolov, A.V. Determination of Methane Dissolved in Water Using Metal-Oxide Sensors. *J. Anal. Chem.* **2023**, *78*, 385–389. [CrossRef]

35. Santos, J.P.; Sanchez-Vicente, C.; Sayago, I. Rare Earth Doped Metal Oxide Sensors for the Detection of Methane at Room Temperature. *Chem. Eng. Trans.* **2024**, *112*, 109–114. [CrossRef]

36. Mirzaei, A.; Alizadeh, M.; Ansari, H.R.; Moayedi, M.; Kordrostami, Z.; Safaeian, H.; Lee, M.L.; Kim, T.-U.; Kim, J.-Y.; Kim, H.W.; et al. Resistive gas sensors for the detection of NH$_3$ gas based on 2D WS$_2$, WSe$_2$, MoS$_2$, and MoSe$_2$: A review. *Nanotechnology* **2024**, *35*, 332002. [CrossRef] [PubMed]

37. Horng, R.H.; Lin, S.H.; Hung, D.R.; Chao, P.H.; Fu, P.K.; Chen, C.H.; Chen, Y.C.; Shao, J.H.; Huang, C.Y.; Tarntair, F.G.; et al. Structure Effect on the Response of ZnGa$_2$O$_4$ Gas Sensor for Nitric Oxide Applications. *Nanomaterials* **2022**, *12*, 3759. [CrossRef]

38. Munusami, V.; Arutselvan, K.; Vadivel, S. Development of High Sensitivity LPG and NO$_2$ Gas Sensor Based ZnGa$_2$O$_4$/Graphene Nanoplates Hybrid Structure—A Novel Approach. *Diam. Relat. Mater.* **2021**, *111*, 108167. [CrossRef]

39. Sousa Filho, I.A.; Dagnone Figueiredo, J.F.; Bouquet, V.; Oliveira, A.L.M.; Lebullenger, R.; Garcia Santos, I.M.; Guilloux-Viry, M.; Merdrignac-Conanec, O.; Weber, I.T. ZnGa$_2$O$_4$ and ZnGa$_2$O$_4$:N Thin Films Applied as Sensors for Detection of Acetaldehyde in Ethanol. *Phys. B Condens. Matter* **2023**, *658*, 414834. [CrossRef]

40. Chen, I.C.; Lin, S.S.; Lin, T.J.; Hsu, C.L.; Hsueh, T.J.; Shieh, T.Y. The Assessment for Sensitivity of a NO$_2$ Gas Sensor with ZnGa$_2$O$_4$/ZnO Core-Shell Nanowires—A Novel Approach. *Sensors* **2010**, *10*, 3057–3072. [CrossRef]

41. Park, S.; An, S.; Mun, Y.; Lee, C. UV-Enhanced Room-Temperature Gas Sensing of ZnGa$_2$O$_4$ Nanowires Functionalized with Au Catalyst Nanoparticles. *Appl. Phys. A* **2014**, *114*, 903–910. [CrossRef]

42. Figaro Engineering Inc. Available online: https://www.figaro.co.jp/en/company/history.html (accessed on 19 February 2025).

43. Tomchenko, A.A. Thick-Film Semiconductor Chemical Sensors. In *Encyclopedia of Sensors*; Grimes, C.A., Dickey, E.C., Pishko, M.V., Eds.; American Scientific Publishers: Stevenson Ranch, CA, USA, 2006; Volume 10, pp. 279–290.

44. Ménil, F.; Coillard, P.; Lucat, C. Critical Review of Nitrogen Monoxide Sensors for Exhaust Gases of Lean Burn Engines. *Sens. Actuators B Chem.* **2000**, *67*, 1–23. [CrossRef]

45. Li, Q.; Zeng, W.; Li, Y. Metal Oxide Gas Sensors for Detecting NO$_2$ in Industrial Exhaust Gas: Recent Developments. *Sens. Actuators B Chem.* **2022**, *359*, 131579. [CrossRef]

46. Aishwarya, K.; Nirmala, R.; Navamathavan, R. Recent Advancements in Liquefied Petroleum Gas Sensors: A Topical Review. *Sens. Int.* **2021**, *2*, 100091. [CrossRef]

47. Luchechko, A.; Zhydachevskyy, Y.; Ubizskii, S.; Kravets, O.; Popov, A.; Rogulis, U.; Elsts, E.; Bulur, E.; Suchocki, A. Afterglow, TL and OSL Properties of Mn^{2+}-Doped $ZnGa_2O_4$ Phosphor. *Sci. Rep.* **2019**, *9*, 9544. [CrossRef] [PubMed]

48. Allix, M.; Chenu, S.; Véron, E.; Poumeyrol, T.; Kouadri-Boudjelthia, E.; Alahrache, S. Considerable Improvement of Long-Persistent Luminescence in Germanium and Tin Substituted $ZnGa_2O_4$. *Chem. Mater.* **2013**, *25*, 1600–1606. [CrossRef]

49. Ueda, J.; Back, M.; Brik, M.G.; Zhuang, Y.; Grinberg, M.; Tanabe, S. Ratiometric Optical Thermometry Using Deep Red Luminescence from $^4T_2$ and ^2E States of Cr^{3+} in $ZnGa_2O_4$ Host. *Opt. Mater.* **2018**, *85*, 510–516. [CrossRef]

50. Chen, Q.L.; Shang, L.B.; Xu, H.M.; Ma, C.G.; Duan, C.K. Multi-Valence and Visible to Near-Infrared Photoluminescence of Manganese in $ZnGa_2O_4$: A First-Principles Study. *J. Phys. Chem. C* **2021**, *125*, 21780–21790. [CrossRef]

51. Shiu, W.T.; Li, X.; Chang, L.Y.; Chen, J.L.; Lin, Y.Y.; Lin, B.H.; Sterbinsky, G.E.; Wu, T.; McLeod, J.A.; Li, L. The Influence of Hydro-Thermal Synthesis Temperature on the Electronic Structure and Luminescence Property of Cr-Doped $ZnGa_2O_4$ Nanoparticles. *J. Lumin.* **2023**, *263*, 120113. [CrossRef]

52. Brik, M.G.; Ma, C.G.; Yamamoto, T.; Piasecki, M.; Popov, A.I. First-Principles Methods as a Powerful Tool for Fundamental and Applied Research in the Field of Optical Materials. In *Phosphor Handbook: Experimental Methods for Phosphor Evaluation and Characterization*; CRC Press: Boca Raton, FL, USA, 2022; pp. 1–26.

53. Mushtaq, U.; Kumar, V. Host-Sensitized Colour-Tunable Emission and Judd-Ofelt Analysis for Dy^{3+}-Doped $ZnGa_2O_4$ Phosphor through Exciton-Mediated Energy Transfer. *Opt. Mater.* **2023**, *146*, 114554. [CrossRef]

54. Suchikova, Y.; Nazarovets, S.; Popov, A.I. Ga_2O_3 Solar-Blind Photodetectors: From Civilian Applications to Missile Detection and Research Agenda. *Opt. Mater.* **2024**, *157*, 116397. [CrossRef]

55. Fritzen, D.L.; Nardy, G.; Portes, M.C.; Giordano, L.; Bonturim, E.; Teixeira, V.C.; Rodrigues, L.C.V. From Synthesis to Fabrication: Engineering Thin Translucent Films with Green Persistent Luminescence Nanoparticles. *Opt. Mater. X* **2023**, *20*, 100271. [CrossRef]

56. Singh, G.; Virpal; Singh, R.C. Highly Sensitive Gas Sensor Based on Er-Doped SnO_2 Nanostructures and Its Temperature Dependent Selectivity towards Hydrogen and Ethanol. *Sens. Actuators B Chem.* **2019**, *282*, 373–383. [CrossRef]

57. Liu, X.; Li, J.; Guo, L.; Wang, G. Highly Sensitive Acetone Gas Sensors Based on Erbium-Doped Bismuth Ferrite Nanoparticles. *Nanomaterials* **2022**, *12*, 3679. [CrossRef] [PubMed]

58. Jiao, M.Z.; Chen, X.Y.; Hu, K.X.; Qian, D.Y.; Zhao, X.H.; Ding, E.J. Recent Developments of Nanomaterials-Based Conductive Type Methane Sensors. *Rare Met.* **2021**, *40*, 1515–1527. [CrossRef]

59. Basu, S.; Basu, P.K. Nanocrystalline Metal Oxides for Methane Sensors: Role of Noble Metals. *J. Sens.* **2009**, *2009*, 861968. [CrossRef]

60. Fu, L.; You, S.; Li, G.; Li, X.; Fan, Z. Application of Semiconductor Metal Oxide in Chemiresistive Methane Gas Sensor: Recent Developments and Future Perspectives. *Molecules* **2023**, *28*, 6710. [CrossRef]

61. Chen, L.; Yu, Q.; Pan, C.; Song, Y.; Dong, H.; Xie, X.; Li, Y.; Liu, J.; Wang, D.; Chen, X. Chemiresistive gas sensors based on electrospun semiconductor metal oxides: A review. *Talanta* **2022**, *246*, 12352. [CrossRef]

62. Kekana, M.T.M.; Mosuang, T.E.; Ntsendwana, B.; Sikhwivhilu, L.M.; Mahladisa, M.A. Notable synthesis, properties and chemical gas sensing trends on molybdenum disulphides and diselenides two-dimensional nanostructures: A critical review. *Chemosphere* **2024**, *366*, 143497. [CrossRef]

63. Chen, M.I.; Singh, A.K.; Chiang, J.L.; Horng, R.H.; Wuu, D.S. Zinc Gallium Oxide—A Review from Synthesis to Applications. *Nanomaterials* **2020**, *10*, 2208. [CrossRef]

64. Wang, Y.P.; Zhang, H.S.; Lin, L.T.; Zhou, S.F.; Yao, Y.; Yang, X.B.; Zhao, Y.J. Role of Intrinsic Defects on the Persistent Luminescence of Pristine and Mn Doped $ZnGa_2O_4$. *J. Appl. Phys.* **2019**, *125*, 095701. [CrossRef]

65. Ponzoni, A.; Baratto, C.; Cattabiani, N.; Falasconi, M.; Galstyan, V.; Nunez-Carmona, E.; Rigoni, F.; Sberveglieri, V.; Zambotti, G.; Zappa, D. Metal Oxide Gas Sensors, a Survey of Selectivity Issues Addressed at the SENSOR Lab, Brescia, Italy. *Sensors* **2017**, *17*, 714. [CrossRef]

66. Almaev, A.V.; Chernikov, E.V.; Davletkildeev, N.A.; Sokolov, D.V. Oxygen Sensors Based on Gallium Oxide Thin Films with Addition of Chromium. *Superlattices Microstruct.* **2020**, *139*, 106392. [CrossRef]

67. Gaman, V.I.; Almaev, A.V. Dependences of Characteristics of Sensors Based on Tin Dioxide on the Hydrogen Concentration and Humidity of Gas Mixture. *Russ. Phys. J.* **2017**, *60*, 90–100. [CrossRef]

68. Gurlo, A. Interplay between O_2 and SnO_2: Oxygen Ionosorption and Spectroscopic Evidence for Adsorbed Oxygen. *ChemPhysChem* **2006**, *7*, 2041–2052. [CrossRef] [PubMed]

69. Sopiha, K.V.; Malyi, O.I.; Persson, C.; Wu, P. Chemistry of Oxygen Ionosorption on SnO_2 Surfaces. *ACS Appl. Mater. Interfaces* **2021**, *13*, 33664–33676. [CrossRef] [PubMed]

70. Cai, Y.; Wilson, M.N.; Beare, J.; Lygouras, C.; Thomas, G.; Yahne, D.R.; Ross, K.M.; Taddei, K.M.; Sala, G.; Dabkowska, H.A.; et al. Crystal Fields and Magnetic Structure of the Ising Antiferromagnet $Er_3Ga_5O_{12}$. *Phys. Rev. B* **2019**, *100*, 184415. [CrossRef]

71. Nogales, E.; García, J.A.; Mendez, B.; Piqueras, J.; Lorenz, K.; Alves, E. Visible and Infrared Luminescence Study of Er Doped β-Ga_2O_3 and $Er_3Ga_5O_{12}$. *J. Phys. D Appl. Phys.* **2008**, *41*, 065406. [CrossRef]

72. Nakayama, A.; Asai, K.; Nagayasu, Y.; Iwamoto, S.; Yagasaki, E.; Inoue, M. Effect of Support Particle Morphology of Ni Catalysts on Growth of Carbon Nanotubes by Methane Decomposition. *J. Jpn. Pet. Inst.* **2006**, *49*, 308–314. [CrossRef]

73. Weber, I.T.; Valentini, A.; Probst, L.F.D.; Longo, E.; Leite, E.R. Catalytic Activity of Nanometric Pure and Rare Earth-Doped SnO_2 Samples. *Mater. Lett.* **2008**, *62*, 1677–1680. [CrossRef]

74. Wolkenstein, T. *Electronic Processes on Semiconductor Surfaces During Chemisorption*; Springer: New York, NY, USA, 1991. [CrossRef]

75. Kozhushner, M.A.; Trakhtenberg, L.I.; Landerville, A.C.; Oleynik, I.I. Theory of Sensing Response of Nanostructured Tin-Dioxide Thin Films to Reducing Hydrogen Gas. *J. Phys. Chem. C* **2013**, *117*, 11562–11568. [CrossRef]

76. Postica, V.; Lupan, O.; Gapeeva, A.; Hansen, L.; Khaledialidusti, R.; Mishra, A.K.; Drewes, J.; Kersten, H.; Faupel, F.; Adelung, R.; et al. Improved Long-Term Stability and Reduced Humidity Effect in Gas Sensing: SiO_2 Ultra-Thin Layered ZnO Columnar Films. *Adv. Mater. Technol.* **2021**, *6*, 2001137. [CrossRef]

77. Fleischer, M.; Seth, M.; Kohl, C.-D.; Meixner, H. A selective H_2 sensor implemented using Ga_2O_3 thin-films which are covered with a gas-filtering SiO_2 layer. *Sens. Actuators B Chem.* **1996**, *36*, 297–302. [CrossRef]

78. Wang, Y.; Zhou, Y. Recent Progress on Anti-Humidity Strategies of Chemiresistive Gas Sensors. *Materials* **2022**, *15*, 8728. [CrossRef]

79. Korotcenkov, G.; Cho, B.K. Instability of Metal Oxide-Based Conductometric Gas Sensors and Approaches to Stability Improvement (Short Survey). *Sens. Actuators B Chem.* **2011**, *156*, 527–538. [CrossRef]

80. Yakovlev, N.N.; Almaev, A.V.; Nikolaev, V.I.; Kushnarev, B.O.; Pechnikov, A.I.; Stepanov, S.I.; Chikiryaka, A.V.; Timashov, R.B.; Scheglov, M.P.; Butenko, P.N.; et al. Low-Resistivity Gas Sensors Based on the In_2O_3-Ga_2O_3 Mixed Compounds Films. *Mater. Today Commun.* **2023**, *34*, 105241. [CrossRef]